Development of hydrogen-selective TiOxNy-Pd composite membrane materials by atomic layer deposition

Clémence Badie, Martin Drobek, Anne Julbe, Christophe Charmette, Jim Cartier, Jean-Manuel Decams, Vincent Astie, Mikhael Bechelany, Lionel Santinacci

▶ To cite this version:

Clémence Badie, Martin Drobek, Anne Julbe, Christophe Charmette, Jim Cartier, et al.. Development of hydrogen-selective TiOxNy-Pd composite membrane materials by atomic layer deposition. Applied Materials Today, 2024, 39, pp.102303. 10.1016/j.apmt.2024.102303 . hal-04648051

HAL Id: hal-04648051
https://hal.science/hal-04648051v1

Submitted on 14 Oct 2024

Development of hydrogen-selective TiO_xN_y-Pd composite membrane materials by atomic layer deposition

Clémence Badie,[1,†] Martin Drobek,[2] Anne Julbe,[2] Christophe Charmette,[2] Jim Cartier[2], Jean-Manuel Decams,[3] Vincent Astie,[3] Mikhael Bechelany,[2,4]and Lionel Santinacci[1,*]*

[1] Aix Marseille Univ, CNRS, CINaM, Marseille, France
[2] Institut Européen des Membranes, IEM – UMR 5635, Univ Montpellier, ENSCM, CNRS, Place Eugène Bataillon, 34095 Montpellier cedex 5, France
[3] Annealsys SAS, 139 rue des Walkyries, Montpellier, France
[4] Gulf University for Science and Technology, GUST, Kuwait

Abstract

This work reports on novel hydrogen (H_2) selective membrane composed of TiO_xN_y-Pd nanocomposite thin films prepared by Atomic Layer Deposition (ALD) on asymmetric porous alumina supports. The nanocomposite combines the robustness of a ceramic matrix, selective gas barrier properties of TiO_xN_y thin layer and specific H_2 sorption/affinity of palladium nanoparticles (Pd NPs). Precise control of the thickness and chemical composition of TiO_xN_y-Pd layer enables to achieve promising H_2 selectivities ($\alpha_{H_2/N_2}\approx 35$ and $\alpha_{H_2/He}\approx 7$) with permeances $\pi_{H_2}\approx 228$ GPU at 390°C. At this temperature, TiO_xN_y crystallites start to form in the initially near-amorphous layer and allow selective transport of H atoms generated during the adsorption-dissociation of H_2 on the Pd NPs. This study clearly stresses the effectiveness of ALD in the formation of quasi-dense H_2-permselective membranes while significantly limiting the production costs by reducing the content of expensive elements, such as Pd. Finally, thanks to the versatility of the ALD technique, the present strategy could be extended to other rational design for applications requiring gas separation or detection.

1. INTRODUCTION

Hydrogen (H_2) is a key molecule for the chemical industry and energy transition. Depending on its source, separation and purification are necessary steps prior to its application. Numerous techniques have been explored including adsorption, cryogenic distillation, catalytic reactions and, more recently, membrane separation and electrochemical processes [1-3]. Pressure swing adsorption and cryogenic distillation are generally very efficient and well-integrated in industry. However, these processes require large equipment, complicated operating conditions leading to high energy consumption and costly maintenance. As a consequence, new purification strategies based on membrane processes have gained interest to provide affordable H_2 streams with the required purity [4-6]. In parallel to the widely studied polymer, hybrid, carbon and ceramic (mainly Si-based or dense perovskites) membranes, particular emphasis has been (and is still) devoted to metal-based membranes [7].

Dense palladium-based membranes (Pd and its alloys) are, by far, the most studied because they catalyze H_2 dissociation at their surface, leading to almost infinite selectivity (ideally 100%) and ultrapure H_2 production [8]. They have been largely investigated, trying to improve their properties: permeability, mechanical and thermo-chemical resistance (including poisoning and embrittlement), lifespan, fabrication reproducibility and cost-efficiency. Self-supported Pd-based membranes (> 50 μm thick) are commercially available since a long time. However, Pd high cost and scarcity coupled to the limited H_2 permeate flux (inversely proportional to the Pd thickness) constrain the range of applications [9]. Numerous studies have thus been carried out on other types of dense metallic membranes, such as those based on Ni, Nb, V and their alloys [10-13]. Unlike to Pd, their H_2 permeability is lower at intermediate temperatures, due to the reduced hydrogen solubility and solid-phase diffusion coefficients. In addition, similar to Pd membranes [14], they might also suffer from poisoning by CO, steam, hydrocarbons or sulfur contaminants, and could also be altered by significant hydrogen embrittlement due to expansion, decohesion and hydride phase transition.

Other strategies have been developed to decrease the quantity of Pd by incorporating/depositing Pd-based thin films (≤ 50 μm) onto a porous support: cold-rolling [15], physical vapor deposition [16-18], chemical vapor deposition [19], electroless plating [20, 21] and more recently atomic layer deposition (ALD) [22, 23]. Several of these approaches have been already up-scaled for the commercial production of reliable Pd-based membranes [24-30].

In parallel to these achievements, further intensive research is on-going to develop new H_2-selective membranes with low Pd loading for application at intermediate temperatures (300-400°C). Composite ceramic membranes containing a dispersion of Pd nanoparticles (NPs) were considered by several groups [22, 31, 32]. In such membranes, the contribution of the support material to the hydrogen transport is a key, although little considered in the literature. Various types of porous inorganic materials (e. g. Vycor® glass, metals or ceramics) have been used as supports for H_2-selective layers. Reported critical attributes of the supports includes porous structure characteristics (mainly pore size/distribution and porosity), surface roughness, mechanical, chemical and thermal stabilities, in addition to the compatibility of its thermal expansion coefficient [33]. Metal supports are robust but usually exhibit large and non-uniform pores, and their surface quality can hardly accommodate very thin (< 5 μm) and uniform films [34, 35]. Thus, asymmetric porous ceramic supports are generally preferred, offering a gradual reduction in pore size from the bulk to the top surface, narrow pore size distribution and high surface quality [33, 36]. The top surface of commercial supports can be improved by chemical and/or mechanical (e. g. polishing) treatments, although the incorporation of an intermediate top-layer is often a preferred alternative. This top-layer might modify the original morphology of the support, mitigate inter-diffusion, improve adhesion of the H_2-selective layer, prevent support corrosion or pre-activate the surface by incorporation of first metal nuclei when considering Pd species deposition [33]. The possible contribution of the intermediate layer to the transport of hydrogen species is usually neglected and most of the Pd-based membranes are deposited on inert (non-reducible) alumina supports. The application of a support material able to change its oxidation state during hydrogen permeation could possibly enhance its transport properties thanks to the hydrogen spillover effect at the Pd/support interfaces [25, 37]. This phenomenon could be particularly attractive to guide the design of novel composite membranes with a dispersion of Pd NPs in close contact with an interactive (reducible) support, such as TiN_x.

The use of TiN as a membrane material is still little explored in the literature [26, 38], despite its appealing physicochemical characteristics, including its metal-like electrical conductivity, high thermal and chemical stability, excellent mechanical wear resistance and relatively low cost [39-41]. It is even envisioned as a hydrogen-impermeable material [42-44] while those works nevertheless measures H transport as a function of film processing condition. Research efforts on TiN have been primarily concentrated on investigating physical or chemical vapor deposition

(PVD and CVD) [45-48], and more recently ALD, with a primary focus on the development of thin films for microelectronics or protective coatings [49, 50]. Advantageously, the thermal expansion coefficient of TiN thin films ($\approx 10.3\times10^{-6}$ °C^{-1} [51]) is close to that of Pd ($\approx 11.8\times10^{-6}$ °C^{-1} [52]), thus ensuring a good thermal stability for the Pd-TiN composite membranes developed in this work.

Taking advantage our previous work on ALD of TiN films [53, 54] and Pd NPs [55, 56], this technique was applied to deposit both materials on asymmetric tubular alumina substrates, thus forming a TiO_xN_y-Pd/Al_2O_3 composite membrane system. ALD is well-known for allowing perfect control of the material thickness at the sub-nanometer scale with excellent uniformity and conformality even on highly tortuous substrates such as the studied alumina supports. [54]

The objective of this work was to optimize the fabrication of uniform TiO_xN_y-Pd composite membrane, with a special focus on achieving high H_2 selectivity and permeability by meticulously tuning their thickness and chemical composition. Commercial tubular membrane supports with a γ-Al_2O_3 top-layer were first coated by ALD of a TiO_xN_y layer ensuring gas tightness at room temperature (RT). Then, Pd NPs were deposited by ALD on such modified substrates, resulting in an original composite TiO_xN_y-Pd/Al_2O_3 membrane system. After comprehensive physicochemical characterizations, gas permeation measurements were carried out at different transmembrane pressures and temperatures, and membrane performance were analyzed with a particular focus on hydrogen selectivity. Promising permselectivities ($\alpha_{H_2/N_2} \approx 35$ and $\alpha_{H_2/He} \approx 7$) were obtained at temperatures of 390°C, with H_2 permeances reaching 228 GPU. The results are discussed and demonstrate the significant role of TiO_xN_y within the gas separation process.

2. MATERIAL AND METHODS

2.1. Membrane

The tubular supports used for TiO_xN_y and Pd depositions were purchased from Pall-Exekia, France. The substrate shown in Figure 1 exhibits an asymmetric porous structure composed of a mesoporous inner top-layer of γ-Al_2O_3 with mean pore sizes between 5 to 8 nm. This layer is deposited on a macroporous tubular support ($\varnothing_{in/out}$ = 7 and 10 mm), consisting of 3 layers with average pore sizes of 0.2 µm, 0.8 µm and 10 µm from the inner to the outer side of the tube. Before ALD, the tube was cut into 50 mm long pieces. To prevent any gas leakage during permeation tests, both ends of the tube were sealed over 10 mm with a commercial enamel at 900°C. The tubular supports were broken for cross sectional observations by scanning electron microscopy (SEM) and chemical analysis by energy-dispersive X-ray spectroscopy (EDS) and X-ray photoelectron spectroscopy (XPS). The pieces used for EDS analysis were embedded in epoxy resin then cut with a diamond wire saw. Several abrasive paper disks and a 1 µm diamond suspension were successively employed to polish the cross-section.

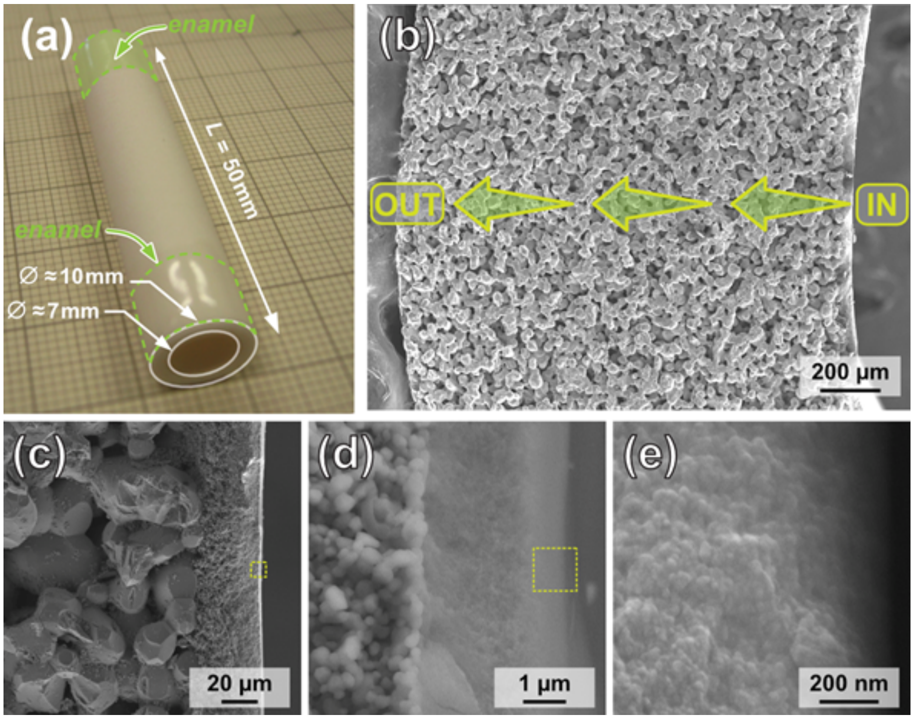

Figure 1: (a) General view of the pristine Al_2O_3 tubular support. (b) SEM image of the tube cross-section. (permeate flow through the tube -from inside to the outside- is indicated by the arrows), (c, d, and e) show progressive enlarged views of the inner part of the tube. The squares plotted in (c) and (d) correspond to the micrographs shown in (d) and (e), respectively.

2.2. Atomic Layer Deposition of TiO_xN_y and Pd

TiO_xN_y and Pd were deposited by ALD reactor (Fiji 200, Veeco/Cambridge Nanotech). TiO_xN_y was deposited using TDMAT (tetrakis(dimethylamino)titanium, 99.99%, Strem Chemicals) as Ti precursor and NH_3 as co-reactant, combined with Ar as carrier gas according to a method described previously [53, 54]. All gases were electronic grade ≥ 99.999%, purchased from Linde Electronics. As previously reported [55,56], Pd deposition was carried out with $Pd(hfac)_2$ (palladium(II)hexafluoroacetylacetonate, 98% from Strem Chemicals) and formalin (37% formaldehyde in water with 10-15% of methanol from Sigma-Aldrich). Containers with Ti and Pd precursors were maintained at 70 and 90°C, respectively, to ensure sufficient vapour pressure. The temperature of the reaction chamber was set to 200°C for both depositions. In addition to the alumina supports, pieces of silicon wafers (n-type Si (100), phosphorus doped, 1-10 Ω·cm, from Sil'tronix, France) were added to each ALD run as a control sample for thickness measurements of all deposited materials. TiO_xN_y and Pd ALD cycles consisted of sequential pulse, exposure, and purge of the metal-precursor and co-reactant, alternatively. The cycle sequences for TiO_xN_y and Pd NPs were: 0.2:3:15/6:3:20 s and 1:30:30/3:30:30 s, respectively. The full description of the deposition protocols is given in Supplementary Information and in Figure S1. The thickness of TiO_xN_y ($t_{TiO_xN_y}$) was tuned by adjusting the number of ALD cycles ($N_{TiO_xN_y}$) and the number of cycles for Pd NPs remained unchanged, $N_{Pd} = 600$ cycles.

2.3. Physico-chemical characterization of materials

TiO_xN_y thickness was monitored by *in situ* spectroscopic ellipsometry (SE) using a M-2000V ellipsometer (J. A. Woollam Co.) and curve fitting was performed using CompleteEASE 5.1 software. SEM and transmission electron microscopy (TEM) were carried out on a JSM 7900F (JEOL Ltd) and a JEM 2100F (JEOL Ltd), respectively, to investigate the morphology of the material, confirm the films thickness and assess their conformality. Chemical analysis of the samples was performed by EDS using a Quantax FlatQuad (Bruker) mounted on the SEM. In addition, a backscattered electron (BSE) detector was operated to obtain SEM images providing chemical rather than morphological contrast generated by the secondary electron (SE) detector. Due to the presence of the γ-Al_2O_3 on the tubular support and the usual X-ray penetration depth (5 to 50 µm depending on the 2θ angle), the TiO_xN_y-Pd nanocomposite is not detected. The analysis of the crystallinity of TiO_xN_y films and Pd NPs is therefore tricky. To overcome this issue, a very thin layer of Al_2O_3 was grown on TEM grids made of a carbon membrane (Holey) at 150°C using a process described elsewhere [57]. The as-prepared grids coated with Al_2O_3 and TiO_xN_y-Pd nanocomposite mimicking the fabricated membranes were then used to characterize the material crystallinity. The selected grids were finally annealed under H_2 atmosphere using an AS-One oven (Annealsys SAS) for 1 h at temperatures ranging from 200 to 400°C under $P = 1$ bar. A first, TiO_xN_y layer was deposited before alumina to ensure that no Cu diffusion from the grid edges will occur (see supplementary materials for detailed description, TEM observation section).

XPS was used to determine the chemical composition of the deposited material. The analysis was carried out on a Kratos Axis Ultra spectrometer (Kratos Analytical, UK) equipped with a monochromatic Al K_α source (1486.6 eV). All spectra were recorded at a take-off angle of 90°, with an analysed area of about 0.7×0.3 mm^2. Survey spectra were collected at 160 eV pass energy with 1.0 eV step. The high-resolution regions were acquired with 0.1 eV step (0.05 eV for O 1s and C 1s) and 20 eV pass energy. A neutralizer was used to compensate for charge effects during the measurement. Curves were fitted using a Gaussian/Lorentzian (70/30) peak shape after Shirley background subtraction and using CasaXPS software (version 2.3). Component peaks were defined by binding energy (BE) and full width at half maximum (FWHM). The carbon C 1s is calibrated at 284.8 eV for the C–C bond.

2.4. Gas permeation measurements

Gas permeance and selectivity measurements were carried out with different single gases (He, H_2, N_2). High-purity H_2 (99.9992%) was supplied by Air Products, while N_2 and He (99.995% and 99.999%, respectively) were provided by Linde gas. The membranes were equipped with silicon or graphite o-rings, placed in a stainless-steel module and degassed before each measurement. A bubble flowmeter connected to the atmosphere, or an electronic flowmeter (PE 1000, Perkin Elmer) was used to measure the gas flow through the membrane and thus determine the permeance values. Ideal selectivities were determined as a ratio of single gas permeances measured in a temperature range of 25-392°C and applying a transmembrane pressure in the range ΔP = 1-3 bar. The stabilization time before each gas flow measurement was generally set at 30 min and gas permeation test was always achieved by applying transmembrane pressures from the highest to the lowest value. The estimated error was determined to be ≈ 12%. Permeance values were expressed in GPU (gas permeation units, where 1 GPU corresponds to $3.3 \cdot 10^{-10}$ mol·m^{-2}·s^{-1}·Pa^{-1}).

3. RESULTS AND DISCUSSION

3.1. Deposition of TiO_xN_y layers

TiO_xN_y deposition was adapted from the ALD protocol described in our previous study [54]. In the present work, exposure time was included to allow efficient diffusion of TDMAT and NH_3 within the mesoporous γ-Al_2O_3 support layer (the TiO_xN_y deposition protocol is described in Figure S1 of Supplementary materials). Figure 2a displays the EDS chemical mapping of Ti for an optimized 120 nm-thick TiO_xN_y layer obtained after $N_{TiO_xN_y}$ = 1000 cycles. Nitrogen was not detected by because it is a light element [58]. This is further confirmed by EDS spectrum performed at low accelerating voltage (E =5 keV) shown in Figure S2 of Supplementary materials. According to this analysis, Ti was detected throughout the support, thus illustrating the efficient diffusion and reaction of TDMAT and NH_3 within the entire porous network. This results in a uniform and conformal coating of the grain surface in both macroporous (α-Al_2O_3) and mesoporous (γ-Al_2O_3) sections of the support. No significant alteration of the porous structure that could have an impact on gas flow occurred in the macropores (pore diameters are significantly larger than the thickness of the deposited layer). Conversely, the mesoporous γ-Al_2O_3 section was fully infiltrated and sealed by the TiO_xN_y deposit. A compact film (indicated by the white arrow in Figure 2a) was indeed formed on the surface of γ-Al_2O_3 (Figure 2b). Such high magnification SEM image suggests that once the γ-Al_2O_3 mesopores are clogged, additional ALD cycles lead to the formation of a pure and compact TiO_xN_y film on the inner surface of the support.

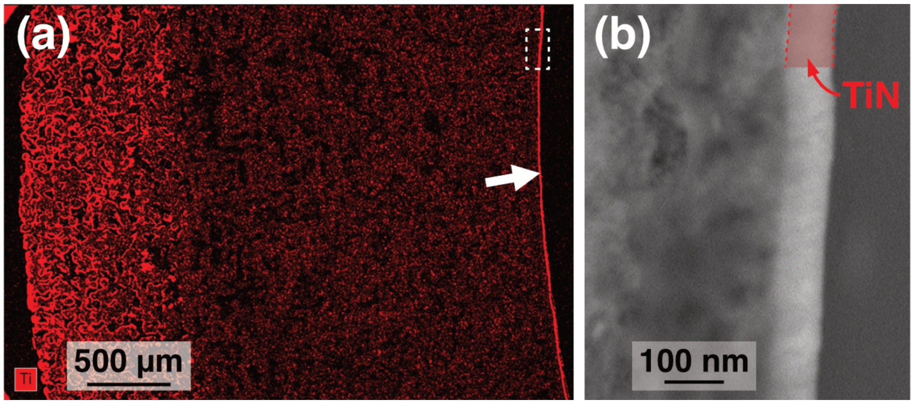

Figure 2: (a) EDS Ti mapping performed on the cross section of the alumina support after TiO_xN_y deposition. Mapping corresponds to Ti K_α transition (E =4.5 keV) using an accelerating voltage of 10 keV. (b) High magnification SEM cross-section of the inner wall of the alumina support corresponding to the dashed rectangle shown in (a). The SEM micrograph is performed using the BSE detector. It therefore reveals the chemical contrast.

The chemical composition of TiO_xN_y was further examined by XPS. The survey spectrum (Figure S3 of Supplementary materials) reveals the expected signals for Ti, N, O and C. The Ti 2p peak of the as-grown thin film is shown in Figure 3a, while the spectra showing N 1s, O 1s, and C 1s are presented in the supplementary materials (Figure S4). The peak of Ti 2p was found to shift toward higher binding energies compared to the value commonly reported for pure Ti–N in the literature (≈ 455 eV) [59]. Hence, the layer should be more accurately classified as an oxynitride (TiN_xO_y) rather than a pure nitride. This is in agreement with the significant amount of detected O. Ti 2p peak consists of two primary contributions at 457.5 (I) and 458.2 eV (II), respectively. The former, located at a lower binding energy, corresponds to a nitrogen-rich oxynitride (*x* > *y*), while the latter is ascribed to an oxygen-rich oxynitride (*x* < *y*) [60-62]. These findings align with the atomic percentages of N and O presented in Table S1. The high oxygen content in the TiO_xN_y layer could be attributed to partial oxidation of the material when exposed to the atmosphere [63, 64]. Figure S2 and Table S2 present an XPS analysis of a TiO_xN_y layer on a Si wafer before and after Ar^+ sputtering. Unlike what we have observed previously during TiN deposition by plasma-enhanced ALD [54], the entire layer contains a significant amount of O after Ar^+ sputtering as shown in Figure S2. Only the C content decreases from 30.9 to 14.7 at.%. The large amount of C at the top surface can easily be ascribed to surface contamination due to TDMAT decomposition at 200°C as reported by Li et al. [65]. On the other hand, no Ti-C bond is observed at 454-455 eV, suggesting that the C content is minor [66].

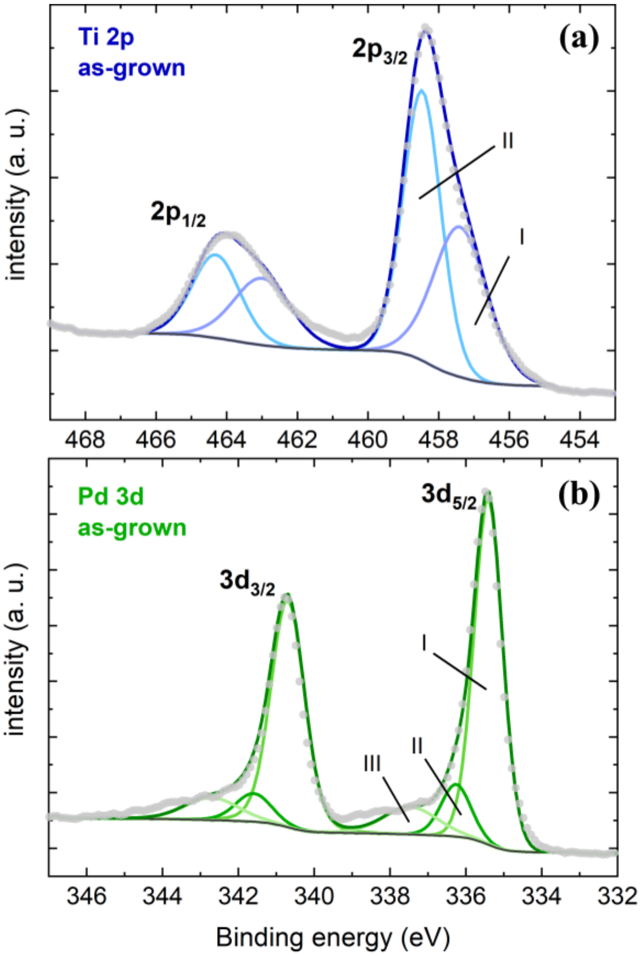

Figure 3: XPS spectra of (a) Ti 2p and (b) Pd 3d of the as-grown TiN-Pd NPs composite.

3.2. Deposition of Pd nanoparticles

TiO_xN_y-coated Al_2O_3 supports were further modified by Pd NPs deposition as active material to facilitate hydrogen transport (H_2 adsorption, dissociation, and diffusion) across the TiO_xN_y layer. Pd was also deposited in exposure mode at the same temperature as TiO_xN_y. Unlike TiO_xN_y, the small amount of deposited Pd NPs did not reach the sensitivity threshold for EDS mapping to provide relevant information regarding the presence of Pd in the porous network. In contrast, SEM and XPS analyses were found to be more suitable for confirming the presence of Pd NPs and their exact chemical composition. In Figure 4a, the SEM observation shows an alumina grain located at the outer section of the support successively coated by TiO_xN_y and Pd NPs. The inset of Figure 4b provides a closer view of the TiO_xN_y films exhibiting some roughness that could be ascribed to Pd NPs. This indicates that Pd NPs are deposited on the outer side of the membrane. It is in line with the high capability of ALD to conformally coat porous materials when a sufficiently long diffusion time is imposed. Finally, Figure 4c clearly demonstrates the presence of Pd NPs on the compact TiO_xN_y layer formed on the inner surface of the membrane. These Pd NPs, indeed, correspond to the approximately 10 nm wide lighter spots revealed by the BSE detector. Pd, with its higher atomic number ($Z_{Pd} = 46$), appears as a brighter feature above the darker underlying TiO_xN_y (average atomic number: $Z_{TiOxNy} \approx 12.3$). This demonstrates that, after ALD of Pd, NPs fully cover the surface of the TiO_xN_y-coated alumina support.

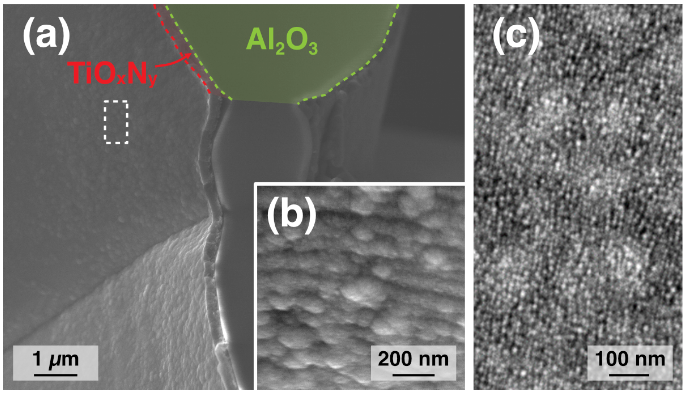

Figure 4: SEM images (BSE detector) of the Al_2O_3 support after TiO_xN_y and Pd deposition: (a) cross section of an external grain, (b) enlarged view of the grain surface as indicated by the rectangle in (a), and (c) top view of the inner compact surface.

The presence of Pd was, further, confirmed by XPS analysis (Figure 3b). The predominant peak in the Pd 3d spectrum at 335.5 eV (I) corresponds to metallic Pd (Pd^0), while two smaller peaks at 336.2 (II) and 337.5 eV (III) can be assigned to PdO and PdO_2, respectively [55, 56, 67, 68]. The presence of PdO may be related to the TiN_xO_y interface, as the initial pulsed Pd precursors react and bind to the underlying layer, which is likely an oxynitride. Considering the size of the Pd NPs, the contribution of binding reactions with the TiN_xO_y interface should not be underestimated. Additionally, some carbon contamination was also detected. The majority of the identified carbon can probably be attributed to its adsorption on the sample surface, as no Ar sputtering was performed. Notably, the analysis revealed almost no evidence of Ti–C or Pd–C bonds in the Ti 2p and Pd 3d spectra, suggesting no unreacted ligands embedded in the composite layer.

3.3 Gas permeation tests

As expected, $t_{TiO_xN_y}$shows a direct impact on the gas permeation characteristics. Table 1 reports the permeance measured as a function of $t_{TiO_xN_y}$. It was found that a $N_{TiO_xN_y}$= 1000 cycles leading to 120 nm-thick TiO_xN_y film (measured on the accompanying silicon wafers samples) is required to render the tubular support gas-tight, and thus ensure the presence of a dense and defect-free TiO_xN_y layer.

Table 1: Permeance values of N_2 and He for different TiO_xN_y membrane thicknesses (T = 25°C and ΔP =3 bar).

$N_{TiO_xN_y}$(cycles)	$t_{TiO_xN_y}$(nm)	N_2 permeance (GPU)	He permeance (GPU)
200	25	∞	∞
400	50	∞	18600
800	100	27	55
1000	120	2	4

The as-qualified coated supports were then functionalized with Pd NPs and their permeance was subsequently measured for the three selected single gas (N_2, He and H_2) at ΔP = 3 bar and different temperatures ranging from 24 to 390°C (Figure S6 in Supplementary materials). No remarkable changes in the permeance values could be detected for the three gases tested at temperatures up to 292°C. This is reported in Figure 5a where the permeance for the three gases is plotted against T. Above this temperature, only the H_2 permeance increased significantly while those of N_2 and He remained stable. The ideal selectivities calculated at ΔP = 3 bar are plotted in Figure 5b. At T = 390°C, $\alpha^*_{\mathrm{He/N_2}}$is 7 while $\alpha^*_{\mathrm{H_2/N_2}}$ reaches 35. Interestingly, after cooling the membrane to RT, its initial permeance values were recovered (Figure S7 in Supplementary materials), thus confirming the stability of the membrane even after its exposure to high temperatures. This work demonstrates that by using a compact TiO_xN_y underlayer prior to growing sparse Pd NPs, a permselectivity in the order of that of pure ALD-Pd-based composite membrane is achievable (i.e. with much lower Pd loading). TiO_xN_y membranes containing sparse Pd NPs with an average diameter of about 10 nm [55] exhibit a permselectivity of $\alpha^*_{H_2/N_2} \approx 35$ and a permeance of 228 GPU (at 390°C). In comparison, dense film made of Pd particles with an average diameter of $\approx$ 90 nm (our previous work) exhibits a permselectivity of $\alpha^*_{H_2/N_2} \approx 23$ and a permeance of 1000 GPU (at 188°C). Due to the high tortuosity of the Al_2O_3 support, it is tricky to calculate the Pd loading precisely but, qualitatively, it is significantly lower for the system in the present work than for the pure Pd/Al_2O_3 composite membranes described earlier [22].Table S3 compares achieved ideal selectivities to those of a selection of dense membranes reported in the literature. A straightforward and rigorous comparison is difficult due to differences within experimental conditions (temperature and pressure, namely). The $\alpha^*_{H_2/N_2}$ values achieved in the present work are of the same order of magnitude as other composite Pd-based and TiN-based membranes reported in the literature (Table S3). It should be noted that, except for the membrane manufactured by Weber et al. [22], the other membranes are micrometers-thick, whereas those fabricated by ALD are nanometers-thick. This makes a significant difference in the quantity of materials used and consequently their cost.

The results suggest that the separation mechanism through the composite TiN-Pd layer does not rely solely on molecular sieving since He does not cross while it exhibits a smaller kinetic diameter (0.26 nm) as compared to H_2 (0.29 nm). This mechanism rather involves a sorption/diffusion phenomenon facilitating the transport of hydrogen and thus increasing the selectivity of the membrane towards H_2 gas. Naturally, such a separation mechanism can only take place for defects-free layers. It is worth pointing out that compared to our previous study dedicated to Pd/Al_2O_3 membranes [22], current TiN-Pd composite exhibits higher thermal stability and better separation efficiency at higher temperature ($\approx$ 400°C). This finding suggests that the TiN-Pd composite requires higher activation energy (heat) to enable H_2 permeance in comparison with a simple Pd/Al_2O_3. The discrepancy is, thus, most likely due to the presence of the TiO_xN_y matrix, which evolves with the temperature, impacting the chemical composition and/or the crystallinity of the material.

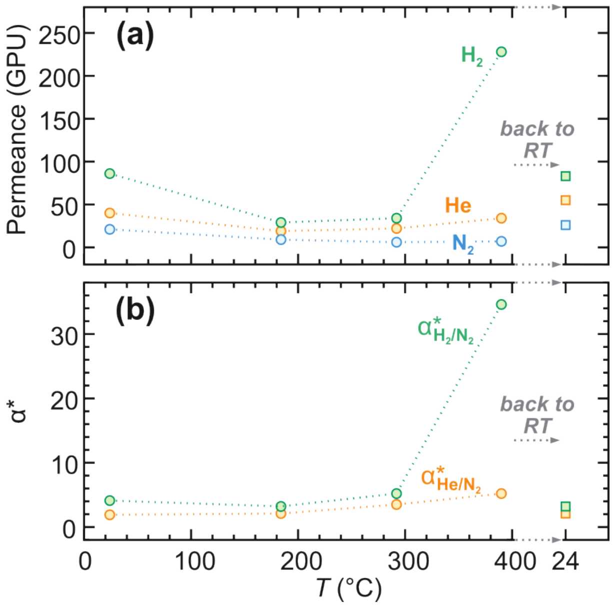

Figure 5: (a) Permeance and (b) ideal selectivities α* for the tested single gases (He, N_2 and H_2) at temperature ranging from 24 to 390°C and $\Delta P = 3$ bar.

3.4 Post-mortem analysis of the TiN-Pd composite layer after H_2 permeation

To gain a better insight into the gas separation mechanism of the TiN-Pd composite layer, a post-mortem analysis was carried out after the series of single gas permeation tests. The XPS analysis of Ti 2p and Pd 3d in the TiN-Pd composite are shown in Figure 6. Figure 6a indicates that the primary Ti 2p contribution in the oxygen-rich oxynitride material TiN_xO_y ($x < y$), as observed before the permeation tests (Figure 3), finally transforms into TiO_2 at 459 eV (II). On the contrary, in the N-rich oxynitride ($x > y$), its intensity decreases but remains at the same energy level, 457.8 eV (I). Although the oxide contributions in the Pd 3d peak feature slightly increases, Pd^0 (I) remains essentially unchanged (Figure 6b). These observations are consistent with the notable rise in oxygen content (Table S1 in Supplementary materials). This finding is somewhat surprising since the H_2 permeation test (pure H_2 at 400°C for 1 h) could be considered as an annealing process in a reducing environment inducing a potential reduction of oxygen/oxide contributions in the material. However, as previously discussed in our previous work [54], annealing in both nitrogen-rich and reducing environments (NH_3 and H_2 at 700°C) was found to be insufficient to lower the presence of TiN_xO_y oxynitride. Therefore, it appears that the applied energy is not high enough to reduce or break the high-energy bonds between Ti and O. In fact, under these conditions only the carbon content is substantially reduced (Table S1). It can therefore be concluded that the main modification of the material is primarily due to the oxidation of its surface when exposed to air rather than to its alteration during H_2 permeation tests.

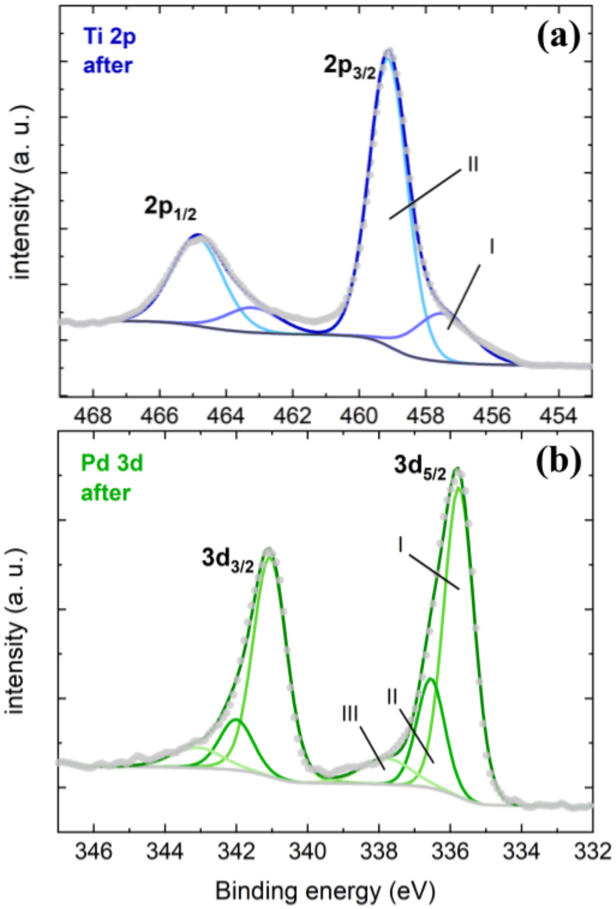

Figure 6: XPS spectra of (a) Ti 2p and (b) Pd 3d after H_2 permeation at 400°C for 1h.

As noted in the previous section, no significant changes in the chemical composition of the material were observed to explain the high H_2 permeance value measured at 390°C. As proposed by Kura et al., the change in material permeability can be attributed to a modification of its morphology and/or crystallinity [26]. In their study, H_2 permeation tests with a favourable evolution of both permeation and selectivity characteristics were carried out using a pure crystalline TiO_xN_y material synthesized by PVD.

To explore this subject further, TiN-Pd layers were also deposited on TEM grids previously coated with an alumina layer (≈ 10 nm thick) deposited by ALD to mimic the ceramic support. Such layers (with TiO_xN_y ≈ 25 nm thick layers and Pd nanoparticles ≈ 5 nm in diameter) were thin enough to allow the electron beam to cross the sample. Schematics of the deposition on the grid is provided in the supplementary materials (Figure S8) together with the description how the SAED patterns were exploited to monitor the crystallinity of the TiO_xN_y -Pd layers. Figure 7a shows that the as-grown TiO_xN_y is slightly polycrystalline, with indexed rings for (111), (200), and (220) planes. On the other hand, each Pd NP is monocrystalline (Figure S8e), but no rings or dots were observed in the SAED images, except for the faint rings located outside the TiO_xN_y ones. After annealing under H_2 atmosphere for 1 h at 200°C and 400°C, the TiO_xN_y signal intensity gradually increases (small dots inside the rings), indicating the growth and formation of crystallites (Figures 7b and 7c). Consistent with the literature, this finding suggests that dissociated hydrogen atoms can pass through the TiO_xN_y layer via its as-formed crystalline structures [26].

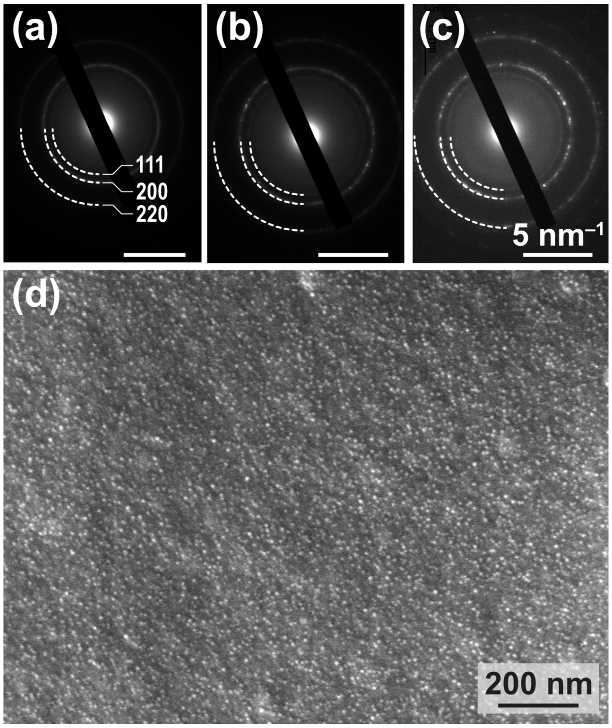

Figure 7: SAED patterns of TiN-Pd deposited on TEM grids, (a) as-grown and annealed under 1 bar H_2 at (b) 200°C and (c) 400°C. SEM micrograph (BSED mode) of the inner surface of the TiN-Pd membrane after permeation tests (d).

Finally, to guarantee the absence of submicrometric surface defects that could possibly appear after H_2 permeation test, a careful examination of the inner surface of the coated support was carried out using SEM. As observed in Figure 7d, no significant changes were detected on the surface compared to the initial membrane state (Figure 3c). Pd NPs remain uniformly dispersed and maintain a constant size (5-10 nm) without any sign of coalescence or dissolution. Figure S9 is showing TEM top view observations of the corresponding TEM grids at room temperature and after treatment at 200 and 400°C presented in Figure 7a-c. Likewise, there was no evidence of dewetting or delamination of the TiO_xN_y layer from the alumina support. It is worth mentioning that unlike Mortaló et al. [38], no cracks or other macroscopic defects in the membrane layer could be detected. This result is consistent with permeation tests conducted both at RT and high-temperatures conditions (i. e. $T = 390°C$), confirming integrity and robustness of the membrane (no viscous flow contribution during permeation tests). As noted previously, Figure 5 (as well as Figure S7 in Supplementary materials) clearly illustrates that, after the high temperature permeation tests, permeance and selectivity return to their initial values measured at RT with the starting composite membrane (as-prepared).

3.5 Suggested gas transport mechanisms

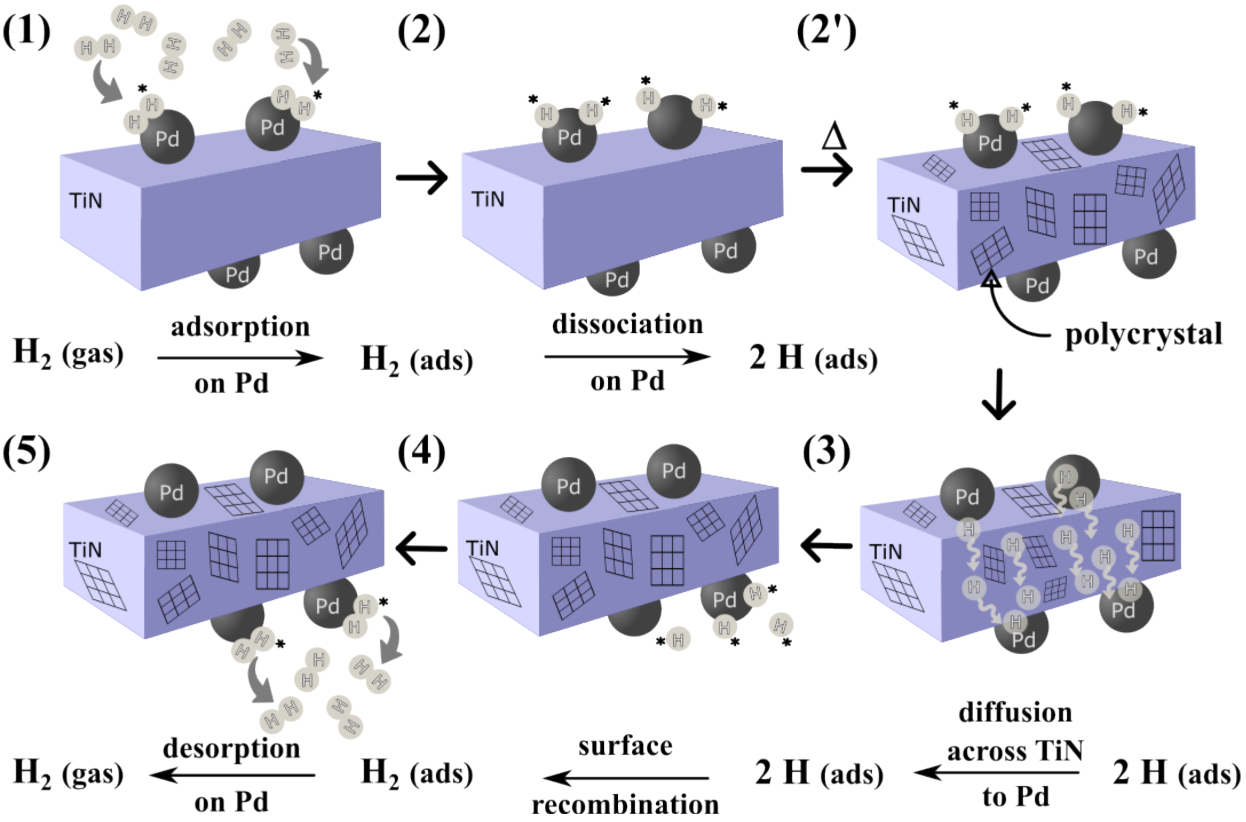

Figure 8: Schematic representation of the H_2 transport mechanism through the TiN-Pd composite membrane layer, highlighting the crucial step of TiO_xN_y crystallization allowing the H diffusion.

A schematic representation of the possible transport mechanisms for hydrogen through the TiN-Pd composite separative layer is proposed in Figure 8. As described elsewhere for dense membranes, the transport mechanism should be based on the solution-diffusion of the targeted species (i. e. H_2) [69]. The process consists of 5 steps: adsorption (1) and dissociation of H_2 molecules on the Pd surface into atomic H (2). Without step (2') which consists of heat the system (Δ) at 390°C, no H dissolution and diffusion through the composite material, as depicted in Figure 5. Heating the system, lead to the formation of TiO_xN_y crystallites, as presented in Figure 7. Once a sufficient crystallinity is reached, step (3), atomic H is transported to across TiO_xN_y can occur. Finally, H atoms recombine (4) and desorb (5) as H_2 molecules on the opposite side of the membrane. This final step (5) can proceed on the Pd NPs present on the other side of the membrane due to the high covering capability of ALD in exposure mode as already demonstrated on TiO_2 nanotubes [55]. It can also be driven and enhanced by the transmembrane pressure, ΔP, between the two sides of the composite layer during the permeation experiments. Pd NPs in contact with the reducible TiO_xN_y matrix are supposed to play a key role by facilitating hydrogen transport through the TiO_xN_y-Pd composite membrane layer. When Pd clusters are nearly saturated with atomic and molecular hydrogen, a possible spillover of the H atoms towards the reducible TiO_xN_y matrix should, indeed, contribute to enhance the H_2 permeance. As reported in [37], the occurrence of spillover phenomenon is well established on reducible supports such as TiO_2, although it is drastically lowered on non-reducible supports such as alumina.

Tracking hydrogen spillover at nanoscale is tricky and requires *in situ* analysis operations. A recent work illustrates the surface-lattice-confinement effect of oxide catalysts, providing a promising route to improve the hydrogen spillover efficiency [25]. The controlled confinement of the Pd NPs in the reducible TiO_xN_y matrix could, indeed, be an attractive prospective to optimise the design of the composite layer for enhancing further the spillover phenomena and thus the permeance of H_2. The evidence of H_2 spillover effect of Pd supported on TiO_xN_y has been recently reported in the field of H_2 sensors [70]. It was shown that a very thin layer of TiO_xN_y provides better sensing performance than pure Pd NPs alone. The literature on the Pd/ TiO_xN_y system is still very limited. A density functional theory (DFT) study by Warczinski et al. reported that nitrogen doping of carbon-supported palladium nanoparticles significantly facilitate the hydrogen spillover reaction [71]. The literature is more abundant for the Pd/TiO_2 system, especially in heterocatalysis. Jin et al. and Tang et al. reported that oxygen vacancies and hydrogen spillover effect by Pd NPs improve the photocatalytic CO_2 reduction [72] and formate electrooxidation [73] performance, respectively.

As demonstrated in Figure 5, high temperatures (T = 390°C) are necessary to allow sufficient permeation of H_2 through the TiN-Pd composite. This threshold is higher than that reported by Weber et al., indicating 200°C for a Pd/Al_2O_3 composite membrane [22]. This finding suggests that in the case of a TiN-Pd composite membrane on Al_2O_3 support the TiO_xN_y layer acts as a barrier material limiting the diffusion of H_2 until the temperature reaches ≈ 390°C. This temperature induces crystallite growth within the poorly crystalline TiO_xN_y layer prepared at lower temperatures. One can therefore conclude that atomic H can only diffuse within the TiO_xN_y layer once a significant degree of crystallinity is reached. This observation is consistent with the findings of Kura et al. [26] and Goncharov et al. [74], who reported that crystalline nitride materials can enable hydrogen permeation/absorption within the grain boundaries interphase (formation of Ti-H terminal groups on the surface of nanocrystallites) [32]. This is in line with the crystal orientation dependence of the permeability of TiO_xN_y films grown by PVD [44]. In this work, thick TiO_xN_y layers ($t_{TiO_xN_y}$= 1 µm) without Pd coating are found impermeable when they are strongly textured according to (200) planes. Note that the polycrystalline nature of the film is however not sufficient for H transport. When returning to RT, H_2 permation is indeed back to its low initial value. This indicates that polycrystalline TiO_xN_y facilitates the H permeation but heat is also requested to activate the process. It is also denoted that a low N/Ti ratio induces some higher H permeability. Previous reports [42], [43] in which H permeation is also performed by electrochemical water reduction already show that low N/Ti ratio in TiN_x leads to a higher H permeability. In all cases, N_2 flow is blocked by such TiN_x PVD layers. This explanation is, however, not sufficient to account for the reversibility of the H permeance. The Pd activation is indeed required to achieve H_2 dissociation to atomic H. The oxynitride nature of the ALD films could also contribute to the H permeation observed in the present study. It is, indeed, a major difference with the previous reports [42-44] and it is also known that H^+ can penetrate in TiO_2 [75, 76]. Such insertion could therefore also occur in TiO_xN_y. Finally, one could also think about H transport through the grain boundaries that could expand at high T and shrink at low T. The mechanism would then be similar to that of a molecular sieve, but the blockage of the He flow denies this explanation.

This mechanistic paragraph mainly considers the role of TiO_xN_y crystallinity to enable the selective transport of hydrogen. Pure Pd or Pd nanoparticles do not require such high temperatures for hydrogen dissociation. According to a study by Mitsui et al., hydrogen can dissociate on a Pd monolayer at just 37 K. They also observed and calculated that a minimum of three active sites is required to enable the dissociation [69].

In addition, it is worth noting that in the field of sensors, which operate on the same principle as selective membranes, hydrogen can be detected at low temperature, including room temperature, as reported by Gupta et al. [77] and Lupan et al. [78].

4. CONCLUSION

This study presents an innovative approach to develop an H_2-selective membrane based on TiO_xN_y-Pd composite layer deposited on porous Al_2O_3 supports. Such a material combines the stability of a ceramic support matrix, the barrier effect of thin TiO_xN_y layers and the specific H_2 sorption/affinity of Pd NPs. The synthesis protocol involves consecutive deposition of thin films of TiO_xN_y and Pd NPs on an asymmetric tubular alumina supports by thermal ALD. The optimized TiO_xN_y thickness blocking the gas flow was 120 nm. After ALD on Pd NPs, gas permeation tests carried out at high operating temperatures ($T = 390°C$) revealed promising permselectivities ($\alpha_{H_2/N_2} \approx 35$ and $\alpha_{H_2/He} \approx 7$) with hydrogen permeances up to 228 GPU. Such permeation is possible because Pd NPs are grown on both sides of the TiO_xN_y compact layer. The elevated temperature was found to be critical for initiating the high permselectivity. This is, first, due to the activation energy required for H dissociation at Pd surface but it could also be ascribed to the crystalline nature of the layer under heating as well as the oxynitride nature of the layer. Further improvement of the membrane performance could be expected by enhancing the spillover phenomenon, thanks to a controlled confinement of the Pd NP in the reducible TiO_xN_y matrix. The performance obtained is in line (same order of magnitude) with the $\alpha^*_{H_2/N_2}$ values reported in the literature for other composite Pd-based and TiN-based membranes reported in the literature. It should be noted that the other H_2-selective composite membranes are usually micrometers-thick, whereas the thickness of the ALD-fabricated ones is in the nanometer range. This makes a significant difference in terms of the amount of materials applied and consequently the membrane cost. This is why ALD is well adapted to operate such a rational design of composite membrane materials (ongoing work).

Accordingly, this study highlights the effectiveness of ALD in designing compact H_2-permselective membrane nanocomposites composed of TiO_xN_y thin layers (around 120 nm) and Pd NPs. The use of low quantities of expensive elements is also expected to significantly reduce membrane production costs. Thus, ALD confirms to be well suited for efficient coating of nanostructured substrates with a precise control of material thickness and composition. These attributes can also be advantageous for microporous devices, allowing surface modifications without affecting the pore network or walls. Following this proof of concept, further investigations are required to confirm the performance of the membranes in real conditions, notably the thermal behavior of the membrane components and their interfaces in H_2 atmosphere during temperature cycling which impact on the membrane stabilization, including in gas mixtures such as N_2, H_2, CO, CO_2, and H_2O present in steam methane reforming or biomass gasification.

CREDIT AUTHOR CONTRIBUTION STATEMENT

Clémence Badie: Conceptualization, Methodology, Investigation, Data curation, Analysis, Writing original draft. **Martin Drobek:** Data curation, Analysis, validation, Writing, Review & Editing. **Anne Julbe:** Analysis, Review & Editing. **Christophe Charmette:** Investigation. **Jim Cartier:** Investigation. **Jean-Manuel Decams:** Investigation, Formal analysis, Review & Editing. **Vincent Astié:** Investigation. **Mikhael Bechelany:** Conceptualization, Funding acquisition, Project management, Analysis, Validation, Writing - Review & Editing. **Lionel Santinacci:** Conceptualization, Funding acquisition, Project management, Supervision, Analysis, Validation, Writing - Review & Editing.

All authors have given approval to the final version of the manuscript.

DECLARATION OF COMPETING INTEREST

The authors declare that they have no known competing financial interests or personal relationships that could have appeared to influence the work reported in this paper.

ACKNOWLEDGMENTS

The authors thank D. Chaudanson, A. Altié and D. Ferry (CINaM) for their valuable help in the electron microscopy measurements as well as O. Grauby (CINaM) for his advice with the sample preparation using epoxy resin. Aurélien Renard (Univ. Lorraine, Nancy, France) is acknowledged for XPS measurements and Maïssa Barr and Prof. Dr. Julien Bachmann (Friedrich-Alexander Univ., Erlangen, Germany) for the XPS with Ar^+ sputtering. This project has been funded by the French National Research Agency (ANR) as part of grant ANR-17-CE09-0049-03 (MENINA project).

SUPPLEMENTARY MATERIALS

Supplementary materials contain details about the TiO_xN_y deposition protocol, EDS spectrum of the membrane after TiO_xN_y and Pd deposition, XPS survey spectrum and N 1s, O 1s, and C 1s, before and after permeance tests (table of the atomic percentages of the main elements). The comparison of single gas permeance values of N_2, He and H_2 in a temperature range from 24 to 390°C are shown as well as the permeance values after cooling the membrane to RT. Schematics of the deposition on the grid together with the description how the SAED patterns were exploited to monitor the crystallinity of the TiO_xN_y-Pd layers and additional TEM pictures.

AUTHOR INFORMATION

Corresponding Author

* E-mail: mikhael.bechelany@umontpellier.fr (M.B.).
* Email : lionel.santinacci@cnrs.fr (L.S.).

Present Addresses

† Laboratoire des Multimatériaux et Interfaces, UMR CNRS 5615, Univ Lyon, Université Claude Bernard Lyon 1, F-69622 Villeurbanne, France.

REFERENCES

[1] L. Vermaak, H. W. J. P. Neomagus, and D. G. Bessarabov, “Recent Advances in Membrane-Based Electrochemical Hydrogen Separation: A Review,” *Membranes*, vol. 11, no. 2, Art. no. 2, Feb. 2021, doi: 10.3390/membranes11020127.

[2] M. Amin *et al.*, “Issues and challenges in hydrogen separation technologies,” *Energy Rep.*, vol. 9, pp. 894–911, Dec. 2023, doi: 10.1016/j.egyr.2022.12.014.

[3] A. Lider *et al.*, “Materials and techniques for hydrogen separation from methane-containing gas mixtures,” *Int. J. Hydrog. Energy*, vol. 48, no. 73, pp. 28390–28411, Aug. 2023, doi: 10.1016/j.ijhydene.2023.03.345.

[4] S. Adhikari and S. Fernando, “Hydrogen Membrane Separation Techniques,” *Ind. Eng. Chem. Res.*, vol. 45, no. 3, pp. 875–881, Feb. 2006, doi: 10.1021/ie050644l.

[5] B. Song and J. A. Forsyth, “CACHET 2: Carbon Capture and Hydrogen Production with Membranes,” *Energy Procedia*, vol. 37, pp. 1050–1059, Jan. 2013, doi: 10.1016/j.egypro.2013.05.201.

[6] H. B. Park, J. Kamcev, L. M. Robeson, M. Elimelech, and B. D. Freeman, “Maximizing the right stuff: The trade-off between membrane permeability and selectivity,” *Science*, vol. 356, no. 6343, p. eaab0530, Jun. 2017, doi: 10.1126/science.aab0530.

[7] S. Bellini, G. Azzato, Y. Sun, F. Gallucci, and A. Caravella, “14 - Metal membranes in hydrogen separation and purification,” in *Current Trends and Future Developments on (Bio-) Membranes*, A. Iulianelli and A. Basile, Eds., Elsevier, 2020, pp. 321–350. doi: 10.1016/B978-0-12-817384-8.00014-5.

[8] B. D. Adams and A. Chen, “The role of palladium in a hydrogen economy,” *Mater. Today*, vol. 14, no. 6, pp. 282–289, Jun. 2011, doi: 10.1016/S1369-7021(11)70143-2.

[9] A. Helmi, F. Gallucci, and M. van Sint Annaland, “Resource scarcity in palladium membrane applications for carbon capture in integrated gasification combined cycle units,” *Int. J. Hydrog. Energy*, vol. 39, no. 20, pp. 10498–10506, Jul. 2014, doi: 10.1016/j.ijhydene.2014.05.009.

[10] A. Santucci, S. Tosti, and A. Basile, “4 - Alternatives to palladium in membranes for hydrogen separation: nickel, niobium and vanadium alloys, ceramic supports for metal alloys and porous glass membranes,” in *Handbook of Membrane Reactors*, vol. 1, A. Basile, Ed., in Woodhead Publishing Series in Energy, vol. 1. , Woodhead Publishing, 2013, pp. 183–217. doi: 10.1533/9780857097330.1.183.

[11] M. D. Dolan, D. M. Viano, M. J. Langley, and K. E. Lamb, “Tubular vanadium membranes for hydrogen purification,” *J. Membr. Sci.*, vol. 549, pp. 306–311, Mar. 2018, doi: 10.1016/j.memsci.2017.12.031.

[12] E. Yan *et al.*, “A novel Nb-based hydrogen purification membrane without catalytic palladium overlayer,” *J. Alloys Compd.*, vol. 875, p. 160103, Sep. 2021, doi: 10.1016/j.jallcom.2021.160103.

[13] M. Wang, Z. Wang, X. Tan, and S. Liu, “Externally self-supported metallic nickel hollow fiber membranes for hydrogen separation,” *J. Membr. Sci.*, vol. 653, p. 120513, Jul. 2022, doi: 10.1016/j.memsci.2022.120513.

[14] K. Kian, C. M. Woodall, J. Wilcox, and S. Liguori, “Performance of Pd-Based Membranes and Effects of Various Gas Mixtures on H2 Permeation,” *Environments*, vol. 5, no. 12, Art. no. 12, Dec. 2018, doi: 10.3390/environments5120128.

[15] S. Tosti, L. Bettinali, and V. Violante, “Rolled thin Pd and Pd–Ag membranes for hydrogen separation and production,” *Int. J. Hydrog. Energy*, vol. 25, no. 4, pp. 319–325, Apr. 2000, doi: 10.1016/S0360-3199(99)00044-0.

[16] S. Tosti, L. Bettinali, S. Castelli, F. Sarto, S. Scaglione, and V. Violante, “Sputtered, electroless, and rolled palladium–ceramic membranes,” *J. Membr. Sci.*, vol. 196, no. 2, pp. 241–249, Feb. 2002, doi: 10.1016/S0376-7388(01)00597-X.

[17] T. A. Peters, M. Stange, and R. Bredesen, “Fabrication of palladium-based membranes by magnetron sputtering,” *Palladium Membr. Technol. Hydrog. Prod. Carbon Capture Appl. Princ. Energy Prod. Appl.*, pp. 1–383, 2014.

[18] T. A. Peters, M. Stange, P. Veenstra, A. Nijmeijer, and R. Bredesen, “The performance of Pd–Ag alloy membrane films under exposure to trace amounts of H2S,” *J. Membr. Sci.*, vol. 499, pp. 105–115, Feb. 2016, doi: 10.1016/j.memsci.2015.10.031.

[19] C.-S. Jun and K.-H. Lee, “Palladium and palladium alloy composite membranes prepared by metal-organic chemical vapor deposition method (cold-wall),” *J. Membr. Sci.*, vol. 176, no. 1, pp. 121–130, Aug. 2000, doi: 10.1016/S0376-7388(00)00438-5.

[20] K. Yoshii, Y. Oshino, N. Tachikawa, K. Toshima, and Y. Katayama, “Electrodeposition of palladium from palladium(II) acetylacetonate in an amide-type ionic liquid,” *Electrochem. Commun.*, vol. 52, pp. 21–24, Mar. 2015, doi: 10.1016/j.elecom.2015.01.003.

[21] D. Alique, M. Imperatore, R. Sanz, J. A. Calles, and M. Giacinti Baschetti, “Hydrogen permeation in composite Pd-membranes prepared by conventional electroless plating and electroless pore-plating alternatives over ceramic and metallic supports,” *Int. J. Hydrog. Energy*, vol. 41, no. 42, pp. 19430–19438, Nov. 2016, doi: 10.1016/j.ijhydene.2016.06.128.

[22] M. Weber *et al.*, “Hydrogen selective palladium-alumina composite membranes prepared by Atomic Layer Deposition,” *J. Membr. Sci.*, vol. 596, p. 117701, Feb. 2020, doi: 10.1016/j.memsci.2019.117701.

[23] C. Lausecker, D. Muñoz-Rojas, and M. Weber, “Atomic layer deposition (ALD) of palladium: from processes to applications,” *Crit. Rev. Solid State Mater. Sci.*, vol. 0, no. 0, pp. 1–23, 2023, doi: 10.1080/10408436.2023.2273463.

[24] “We’re enabling the green transition by realising the potential of hydrogen. Here’s how.,” Hydrogen Mem-Tech AS. Accessed: Dec. 05, 2023. [Online]. Available: https://hydrogen-mem-tech.com/

[25] Y. Liu *et al.*, “Direct observation of accelerating hydrogen spillover via surface-lattice-confinement effect,” *Nat. Commun.*, vol. 14, no. 1, Art. no. 1, Feb. 2023, doi: 10.1038/s41467-023-36044-8.

[26] C. Kura *et al.*, “Hydrogen separation by nanocrystalline titanium nitride membranes with high hydride ion conductivity,” *Nat. Energy*, vol. 2, no. 10, Art. no. 10, Oct. 2017, doi: 10.1038/s41560-017-0002-2.

[27] “Johnson Matthey Technology Review,” technology.matthey.com. Accessed: Dec. 05, 2023. [Online]. Available: https://technology.matthey.com

[28] “Optical black light absorbing and coatings,” Acktar black coatings. Accessed: Dec. 05, 2023. [Online]. Available: https://acktar.com/

[29] “Hysep – Hydrogen Separation Modules.” Accessed: Dec. 05, 2023. [Online]. Available: https://www.hysep.com/

[30] “Membrane Purifiers for Europe – NORAM Engineering and Constructors Ltd.” Accessed: Dec. 05, 2023. [Online]. Available: https://www.noram-eng.com/membrane-purifiers-for-europe/

[31] D. A. Pacheco Tanaka *et al.*, “Fabrication of Hydrogen-Permeable Composite Membranes Packed with Palladium Nanoparticles,” *Adv. Mater.*, vol. 18, no. 5, pp. 630–632, 2006, doi: 10.1002/adma.200501900.

[32] A. L. Ahmad, M. A. T. Jaya, C. J. C. Derek, and M. A. Ahmad, “Synthesis and characterization of TiO2 membrane with palladium impregnation for hydrogen separation,” *J. Membr. Sci.*, vol. 366, no. 1, pp. 166–175, Jan. 2011, doi: 10.1016/j.memsci.2010.09.056.

[33] D. Alique, D. Martinez-Diaz, R. Sanz, and J. A. Calles, “Review of Supported Pd-Based Membranes Preparation by Electroless Plating for Ultra-Pure Hydrogen Production,” *Membranes*, vol. 8, no. 1, Art. no. 1, Mar. 2018, doi: 10.3390/membranes8010005.

[34] L. Furones and D. Alique, “Interlayer Properties of In-Situ Oxidized Porous Stainless Steel for Preparation of Composite Pd Membranes,” *ChemEngineering*, vol. 2, no. 1, Art. no. 1, Mar. 2018, doi: 10.3390/chemengineering2010001.

[35] D. Alique, P. Leo, D. Martinez-Diaz, J. A. Calles, and R. Sanz, “Environmental and cost assessments criteria for selection of promising palladium membranes fabrication strategies,” *Int. J. Hydrog. Energy*, May 2023, doi: 10.1016/j.ijhydene.2023.04.292.

[36] N. de Nooijer *et al.*, “Long-Term Stability of Thin-Film Pd-Based Supported Membranes,” *Processes*, vol. 7, no. 2, Art. no. 2, Feb. 2019, doi: 10.3390/pr7020106.

[37] W. Karim *et al.*, “Catalyst support effects on hydrogen spillover,” *Nature*, vol. 541, no. 7635, Art. no. 7635, Jan. 2017, doi: 10.1038/nature20782.

[38] C. Mortalò *et al.*, “Production Strategies of TiNx Coatings via Reactive High Power Impulse Magnetron Sputtering for Selective H2 Separation,” *Membranes*, vol. 11, no. 5, Art. no. 5, May 2021, doi: 10.3390/membranes11050360.

[39] P. Patsalas and S. Logothetidis, “Optical, electronic, and transport properties of nanocrystalline titanium nitride thin films,” *J. Appl. Phys.*, vol. 90, no. 9, pp. 4725–4734, Nov. 2001, doi: 10.1063/1.1403677.

[40] V. K. Prokudina, “Titanium Nitride,” in *Concise Encyclopedia of Self-Propagating High-Temperature Synthesis*, I. P. Borovinskaya, A. A. Gromov, E. A. Levashov, Y. M. Maksimov, A. S. Mukasyan, and A. S. Rogachev, Eds., Amsterdam: Elsevier, 2017, pp. 398–401. doi: 10.1016/B978-0-12-804173-4.00160-5.

[41] S. Datta, M. Das, V. K. Balla, S. Bodhak, and V. K. Murugesan, “Mechanical, wear, corrosion and biological properties of arc deposited titanium nitride coatings,” *Surf. Coat. Technol.*, vol. 344, pp. 214–222, Jun. 2018, doi: 10.1016/j.surfcoat.2018.03.019.

[42] T. Nishikiori, T. Nohira, and Y. Ito, “Hydrogen Impermeability of TiN Films and Its Dependence on Nitrogen Concentration at High Temperatures,” *J. Electrochem. Soc.*, vol. 148, no. 1, p. E52, Jan. 2001, doi: 10.1149/1.1344551.

[43] T. Nishikiori, T. Nohira, and Y. Ito, “Electrochemical evaluation of high temperature hydrogen impermeability of TiN films and its dependence on film thickness,” *Thin Solid Films*, vol. 408, no. 1, pp. 148–154, Apr. 2002, doi: 10.1016/S0040-6090(02)00053-6.

[44] T. Zhou, D. Liu, Y. Zhang, T. Ouyang, and J. Suo, “Microstructure and hydrogen impermeability of titanium nitride thin films deposited by direct current reactive magnetron sputtering,” *J. Alloys Compd.*, vol. 688, pp. 44–50, Dec. 2016, doi: 10.1016/j.jallcom.2016.06.278.

[45] H. de Baynast, A. Bouteville, and J.-C. Remy, “Optimization of Titanium Nitride Rapid Thermal CVD Process,” *Chem. Vap. Depos.*, vol. 6, no. 3, pp. 115–119, 2000, doi: 10.1002/(SICI)1521-3862(200006)6:3<115::AID-CVDE115>3.0.CO;2-G.

[46] H. C. M. Knoops *et al.*, “Deposition of TiN and TaN by Remote Plasma ALD for Cu and Li Diffusion Barrier Applications,” *J. Electrochem. Soc.*, vol. 155, no. 12, p. G287, Oct. 2008, doi: 10.1149/1.2988651.

[47] M.-D. Cheng, T. Luoh, C.-T. Su, T.-H. Yang, K.-C. Chen, and C.-Y. Lu, “Improvement of the properties and electrical performance on TiCl4-based TiN film using sequential flow chemical vapor deposition process,” *Thin Solid Films*, vol. 518, no. 8, pp. 2285–2289, Feb. 2010, doi: 10.1016/j.tsf.2009.10.013.

[48] A. Shearrow *et al.*, “Atomic layer deposition of titanium nitride for quantum circuits,” *Appl. Phys. Lett.*, vol. 113, no. 21, p. 212601, Nov. 2018, doi: 10.1063/1.5053461.

[49] T. Stein and Y. Ein-Eli, “Proton exchange membrane (PEM) fuel cell bipolar plates prepared from a physical vapor deposition (PVD) titanium nitride (TiN) coated AISI416 stainless-steel,” *SN Appl. Sci.*, vol. 1, no. 11, p. 1420, Oct. 2019, doi: 10.1007/s42452-019-1475-3.

[50] J.-Z. Kong, P. Xu, Y.-Q. Cao, A.-D. Li, Q.-Z. Wang, and F. Zhou, “Improved corrosion protection of CrN hard coating on steel sealed with TiOxNy-TiN composite layers,” *Surf. Coat. Technol.*, vol. 381, p. 125108, Jan. 2020, doi: 10.1016/j.surfcoat.2019.125108.

[51] Z. H. Cen *et al.*, “Temperature effect on titanium nitride nanometer thin film in air,” *J. Phys. Appl. Phys.*, vol. 50, no. 7, p. 075105, Jan. 2017, doi: 10.1088/1361-6463/aa54e6.

[52] “Thermal Expansion - Linear Expansion Coefficients.” Accessed: Dec. 05, 2023. [Online]. Available: https://www.engineeringtoolbox.com/linear-expansion-coefficients-d_95.html

[53] L. Assaud, K. Pitzschel, M. Hanbücken, and L. Santinacci, “Highly-Conformal TiN Thin Films Grown by Thermal and Plasma-Enhanced Atomic Layer Deposition,” *ECS J. Solid State Sci. Technol.*, vol. 3, no. 7, p. P253, Jun. 2014, doi: 10.1149/2.0141407jss.

[54] C. Badie *et al.*, “Conductive TiN thin films grown by plasma-enhanced atomic layer deposition: Effects of N-sources and thermal treatments,” *J. Vac. Sci. Technol. A*, vol. 41, no. 3, p. 032401, May 2023, doi: 10.1116/6.0002288.

[55] L. Assaud *et al.*, “Atomic Layer Deposition of Pd Nanoparticles on TiO2 Nanotubes for Ethanol Electrooxidation: Synthesis and Electrochemical Properties,” *ACS Appl. Mater. Interfaces*, vol. 7, no. 44, pp. 24533–24542, Nov. 2015, doi: 10.1021/acsami.5b06056.

[56] M. K. S. Barr *et al.*, “Enhancement of Pd Catalytic Activity toward Ethanol Electrooxidation by Atomic Layer Deposition of SnO2 onto TiO2 Nanotubes,” *J. Phys. Chem. C*, vol. 121, no. 33, pp. 17727–17736, Aug. 2017, doi: 10.1021/acs.jpcc.7b05799.

[57] P. Roy *et al.*, “Preventing Corrosion of Aluminum Metal with Nanometer-Thick Films of Al2O3 Capped with TiO2 for Ultraviolet Plasmonics,” *ACS Appl. Nano Mater.*, vol. 4, no. 7, pp. 7199–7205, Jul. 2021, doi: 10.1021/acsanm.1c01160.

[58] Yougui Liao “Practical Electron Microscopy and Database - An Online Book.” Accessed: May 30, 2024. [Online]. Available: https://www.globalsino.com/EM/

[59] D. Gall *et al.*, “In situ X-ray Photoelectron, Ultraviolet Photoelectron, and Auger Electron Spectroscopy Spectra from First-Row Transition-Metal Nitrides: ScN, TiN, VN, and CrN,” *Surf. Sci. Spectra*, vol. 7, no. 3, pp. 167–168, Jul. 2000, doi: 10.1116/1.1360984.

[60] C. Ernsberger, J. Nickerson, A. E. Miller, and J. Moulder, “Angular resolved x-ray photoelectron spectroscopy study of reactively sputtered titanium nitride,” *J. Vac. Sci. Technol. Vac. Surf. Films*, vol. 3, no. 6, pp. 2415–2418, Nov. 1985, doi: 10.1116/1.572849.

[61] N. C. Saha and H. G. Tompkins, “Titanium nitride oxidation chemistry: An x-ray photoelectron spectroscopy study,” *J. Appl. Phys.*, vol. 72, no. 7, pp. 3072–3079, Oct. 1992, doi: 10.1063/1.351465.

[62] K. Hansen, M. Cardona, A. Dutta, and C. Yang, “Plasma Enhanced Atomic Layer Deposition of Plasmonic TiN Ultrathin Films Using TDMATi and NH3,” *Materials*, vol. 13, no. 5, Art. no. 5, Jan. 2020, doi: 10.3390/ma13051058.

[63] J. S. Colligon *et al.*, “Composition and chemical state of titanium nitride films obtained by different methods,” *Surf. Coat. Technol.*, vol. 70, no. 1, pp. 9–17, Nov. 1994, doi: 10.1016/0257-8972(94)90068-X.

[64] A. M. Kia *et al.*, “Spectroscopic analysis of ultra-thin TiN as a diffusion barrier for lithium-ion batteries by ToF-SIMS, XPS, and EELS,” *Appl. Surf. Sci.*, vol. 564, p. 150457, Oct. 2021, doi: 10.1016/j.apsusc.2021.150457.

[65] W.-M. Li, “Recent Developments of Atomic Layer Deposition Processes for Metallization,” *Chem. Vap. Depos.*, vol. 19, no. 4–6, pp. 82–103, 2013, doi: 10.1002/cvde.201300052.

[66] J. Luthin and C. Linsmeier, “Characterization of electron beam evaporated carbon films and compound formation on titanium and silicon,” *Phys. Scr.*, vol. 2001, no. T91, p. 134, Jan. 2001, doi: 10.1238/Physica.Topical.091a00134.

[67] M. C. Militello and S. J. Simko, “Elemental Palladium by XPS,” *Surf. Sci. Spectra*, vol. 3, no. 4, pp. 387–394, Oct. 1994, doi: 10.1116/1.1247783.

[68] G. A. Shafeev, J. -M. Themlin, L. Bellard, W. Marine, and A. Cros, “Enhanced adherence of area-selective electroless metal plating on insulators,” *J. Vac. Sci. Technol. Vac. Surf. Films*, vol. 14, no. 2, pp. 319–326, Mar. 1996, doi: 10.1116/1.579895.

[69] T. Mitsui, M. K. Rose, E. Fomin, D. F. Ogletree, and M. Salmeron, “Dissociative hydrogen adsorption on palladium requires aggregates of three or more vacancies,” *Nature*, vol. 422, no. 6933, pp. 705–707, Apr. 2003, doi: 10.1038/nature01557.

[70] C. Badie *et al.*, “Enhanced sensitivity towards hydrogen by a TiN interlayer in Pd-decorated SnO $_2$ nanowires,” *J. Mater. Chem. A*, vol. 11, no. 23, pp. 12202–12213, 2023, doi: 10.1039/D3TA00020F.

[71] L. Warczinski and C. Hättig, “How Nitrogen Doping Affects Hydrogen Spillover on Carbon-Supported Pd Nanoparticles: New Insights from DFT,” *J. Phys. Chem. C*, vol. 125, no. 17, pp. 9020–9031, May 2021, doi: 10.1021/acs.jpcc.0c11412.

[72] J. I. A. Xin, L. I. Jinyu, D. Shihao, S. Qianqian, J. I. A. Husheng, and X. U. E. Jinbo, “Synergy Effect of Pd Nanoparticles and Oxygen Vacancies for Enhancing TiO2 Photocatalytic CO2 Reduction,” *J. Inorg. Mater.*, vol. 38, no. 11, p. 1301, Jul. 2023, doi: 10.15541/jim20230170.

[73] Z. Tang *et al.*, “Interfacial Hydrogen Spillover on Pd-TiO2 with Oxygen Vacancies Promotes Formate Electrooxidation,” *ACS Energy Lett.*, vol. 8, no. 9, pp. 3945–3954, Sep. 2023, doi: 10.1021/acsenergylett.3c01426.

[74] A. Goncharov, A. Guglya, A. Kalchenko, E. Solopikhina, V. Vlasov, and E. Lyubchenko, “Nanocrystalline Porous Hydrogen Storage Based on Vanadium and Titanium Nitrides,” *J. Nanotechnol.*, vol. 2017, p. e4106067, Jan. 2017, doi: 10.1155/2017/4106067.

[75] L. A. Lyon and J. T. Hupp, “Energetics of the Nanocrystalline Titanium Dioxide/Aqueous Solution Interface: Approximate Conduction Band Edge Variations between H0 = −10 and H- = +26,” *J. Phys. Chem. B*, vol. 103, no. 22, pp. 4623–4628, Jun. 1999, doi: 10.1021/jp9908404.

[76] M. E. Dufond, J.-N. Chazalviel, and L. Santinacci, “Electrochemical Stability of n-Si Photoanodes Protected by TiO2 Thin Layers Grown by Atomic Layer Deposition,” *J. Electrochem. Soc.*, vol. 168, no. 3, p. 031509, Mar. 2021, doi: 10.1149/1945-7111/abeaf3.

[77] D. Gupta *et al.*, “A low temperature hydrogen sensor based on palladium nanoparticles,” *Sens. Actuators B Chem.*, vol. 196, pp. 215–222, Jun. 2014, doi: 10.1016/j.snb.2014.01.106.

[78] O. Lupan, V. Postica, F. Labat, I. Ciofini, T. Pauporté, and R. Adelung, “Ultra-sensitive and selective hydrogen nanosensor with fast response at room temperature based on a single Pd/ZnO nanowire,” *Sens. Actuators B Chem.*, vol. 254, pp. 1259–1270, Jan. 2018, doi: 10.1016/j.snb.2017.07.200.